A Porous Au@Rh Bimetallic Core-Shell Nanostructure as an H_2O_2-Driven Oxygenerator to Alleviate Tumor Hypoxia for Simultaneous Bimodal Imaging and Enhanced Photodynamic Therapy

Jinping Wang,[1] Jingyu Sun,[2] Wei Hu,[2] Yuhao Wang,[1] Tsengming Chou,[3] Beilu Zhang,[2] Qiang Zhang,[4] Lei Ren,[4] Hongjun Wang*[,1,2]

[1] Department of Biomedical Engineering, Stevens Institute of Technology, Hoboken, New Jersey, 07030, United States

[2] Department of Chemistry and Chemical Biology, Stevens Institute of Technology, Hoboken, New Jersey, 07030, United States

[3] Laboratory for Multiscale Imaging, Stevens Institute of Technology, Hoboken, New Jersey, 07030, United States

[4] Department of Biomaterials, Key Laboratory of Biomedical Engineering of Fujian Province, State Key Lab of Physical Chemistry of Solid Surface, College of Materials, Xiamen University, Xiamen, Fujian 361005, P. R. China

*Corresponding author at: Department of Biomedical Engineering, Stevens Institute of Technology, Hoboken, New Jersey, 07030, United States.

Tel.: +1-201-2165556

E-mail address: hongjun.wang@stevens.edu

Materials and methods

Materials

Sodium hexachlororhodate(III) (Na_3RhCl_6), singlet oxygen sensor green (SOSG), and $[Ru(dpp)_3]Cl_2$ (RDPP) were purchased from Fisher Scientific (Hampton, NH, USA). Poly(ethylene oxide)-b-poly(methyl methacrylate) ($PEO_{(10500)}$-b-$PMMA_{(18000)}$) was obtained from Polymer Source Inc (Dorval, QC, Canada). Tetrachloroauric acid trihydrate ($HAuCl_4 \cdot 3H_2O$), ascorbic acid (AA), and calcein AM/PI stain kit were purchased from Sigma-Aldrich (St. Louis, MO, USA). All chemicals were used as received without further treatment.

Synthesis of porous Au@Rh core-shell nanostructure

Porous Au@Rh core-shell nanostructures were synthesized using a modified soft template method.[1] In a typical synthesis setup, 6 mg of $PEO_{(10500)}$-b-$PMMA_{(18000)}$ was dissolved in 1.2 mL N,N-dimethylformamide (DMF). Then, 0.8 mL of deionized (D.I.) water, 2 mL of Rh and Au precursor mixed solution including 0.4 mL of aqueous 200 mM Na_3RhCl_6 and 1.6 mL of aqueous 15 mM $HAuCl_4 \cdot 3H_2O$, and 2 mL of aqueous 100 mM AA were sequentially added to the above DMF solution to form a transparent light-red solution. The color then rapidly changed to purple red. The reaction solution was kept in 60 °C water bath for 12 h until it turned to black. The nanostructures were collected by centrifugation at 13,000 rpm for 20 min and the residual $PEO_{(10500)}$-b-$PMMA_{(18000)}$ was removed by several consecutive washing/centrifugation cycles with acetone and water. The obtained product was stored at room temperature for further use. Similarly, porous Rh and porous core-shell Au@Pt nanostructures were also prepared for the catalytic capability comparison.

Extraction of tumor cell membrane

Breast cancer cells (MDA-MB-231 cell line) grown to about 80% confluence were

trypsinized and centrifuged at 1,000 rpm for 5 min to form the cell pellet. After washing with phosphate buffered saline (PBS) twice, the cell pellet was then suspended in a hypotonic lysis buffer containing membrane protein extraction reagent. The suspended cell solution was kept in an ice bath for 20-30 min and then sonicated for 5 s to break the cells. Upon centrifugation (8,000 rpm) for 5 min at 4 °C, the supernatant was collected and subjected to further centrifugation at 13,000 rpm for 10 min to collect cell membrane fragments in the supernatant. The collected supernatant containing cell membrane was stored at -20 °C for further use.

Preparation of Au@Rh-ICG-CM nanocomposite

The selected photosensitizer ICG was loaded into the mesopores of Au@Rh nanostructures and then cell membrane (CM) of MDA-MB-231 cells as a gate keeper was coated onto the nanoparticles to trap the ICG molecules. The detailed steps were as follows: 0.1 mg of ICG and 0.5 mg of Au@Rh nanostructures were dissolved in a dimethylsulfoxide (DMSO)/water (v/v = 1:4) solution (1 mL), and stirred at room temperature for 12 h. Then 1 mL of cell membrane solution was added into the above solution and sonicated for 20 min. Next, the obtained mixed solution was centrifuged at 13,000 rpm for 15 min to remove excessive ICG and further washed several times with D.I. water. The final Au@Rh-ICG-CM was dispersed in D.I. water or PBS.

Characterization

Transmission electron microscopic (TEM) imaging was taken with an FEI Titan Themis 200 TEM at an acceleration voltage of 200 kV. Scanning electron microscopic (SEM) images were obtained using a Zeiss Auriga FIB-SEM. UV-vis-NIR absorption spectra were obtained with a multi-detection microplate reader (BioTek Instruments, Inc., Winooski, VT). The wide-angle powder X-ray diffraction (XRD) pattern was recorded using an X-ray diffractometer (X′pert) with an Cu Kα (1.5406 Å) X-ray

source at 40 kV and 40 mA and a scan rate of 5° (2θ)/min (scan range: 30-90°). The low-angle powder XRD pattern was recorded using an Ultima IV diffractometer (M/s, Rigaku Corporation, Japan) with the Ni-filtered Cu Kα radiation (λ= 1.54178 Å). The size and zeta-potential of various nanostructures were determined by dynamic light scattering (Zetasizer 3000HS; Malvern Instruments, Worcestershire, UK). The surface area and pore size of the nanostructures were determined by Brunauer-Emmett-Teller (BET), nitrogen adsorption-desorption and Barrett-Joyner-Halenda (BJH) methods (Micromeritics, ASAP 2010), respectively. The pore volume date was calculated automatically by the software using BJH model.[2] Sodium dodecyl sulfate-polyacrylamide gel electrophoresis (SDS-PAGE) was used to further assess the protein components of CM coated on Au@Rh. Au@Rh, CM vesicles and Au@Rh-CM were prepared in the SDS buffer and measured using a bicinchoninic acid (BCA) kit (Sigma-Aldrich, USA). The samples were heated at 95 °C for 5 min and then 30 μg of each sample was loaded into a 10% SDS gel. The electrophoresis was run at 120 V for 2 h, stained with Commassie blue for 2 h, and then washed overnight before observation. To determine the loading efficiency of ICG in Au@Rh-CM, the mixture of Au@Rh-CM and ICG was centrifuged at 13,000 rpm for 15 min to separate the free ICG from that loaded and then further washed with D.I. water for several times. The non-trapped ICG collected in the supernatant was determined using a multi-detection microplate reader (BioTek Instruments, Inc., Winooski, VT) with an excitation at 590 nm and an emission at 645 nm. Drug loading efficiency (%) = ((weight of loaded drug)/(total weight of nanoparticles)) × 100. An 808-nm multimode pump laser (Shanghai Connect Fiber Optics Co. Ltd., Shanghai, China) was used as the irradiation source for photothermal effect. For *in vitro* PA imaging, Au@Rh-ICG-CM with different concentrations (0, 0.1, 0.2, 0.4, 0.8 and 1.0 mg/mL) were added into 200 μL tubes for

PA signal detection using a PA instrument (VisualSonics Vevo 2100 LAZER systems, FUJIFILM VisualSonics Inc., Toronto, ON, Canada) with an excitation wavelength at 808 nm.

The catalase-like activity of Au@Rh-CM

The catalase-like activity assays were performed at 37 ºC using the Goth method.[3, 4] To evaluate its Michaelis-Menten constant (*K*m), catalytic constants (*K*cat), and maximum reaction velocity (*V*max), 0.02 mL of the as-prepared Au@Rh solution (0.2 mM) was added into 0.1 mL pre-warmed phosphate buffer solution (67 mM) containing H_2O_2 and kept at 37 ºC for 1 min. Then, 0.1 mL ammonium molybdate solution (Mo = 240 mM) was added into the reaction mixture and right away the absorbance at 405 nm was measured using a microplate reader. The *K*m, *V*max and *K*cat of Au@Rh were calculated using the Lineweaver-Burk plot. Besides, the *K*m, *V*max and *K*cat of Rh and Au@Pt nanoparticles with similar porous structures were also measured following the same conditions.

Next, the catalase-like activity of Au@Rh-CM was evaluated by monitoring oxygen generation through catalytic decomposition of hydrogen peroxide. Tubes containing 1) H_2O_2 (20 mM), 2) Au@Rh-CM (50 μg/mL), or 3) Au@Rh-CM (50 μg/mL) + H_2O_2 (20 mM) were allowed to react for 30 min, and then photos were taken.

O_2 production was also evaluated with an oxygen indicator, RDPP, of which the fluorescence intensity decreased with increases of oxygen concentration.[5] Aqueous solutions containing H_2O, H_2O_2, Au@Rh-CM, or Au@Rh-CM + H_2O_2 was added into separate tubes. The concentration of H_2O_2 was 1×10^{-4} M. Then, 0.2 mL of oil was added on top of each tested solution to isolate it from the air. The fluorescence intensity of RDPP (λ_{ex}= 560 nm) at 645 nm was recorded at different time points.

The H_2O_2 decomposition experiment was carried out by adding Au@Rh-CM (50

μg/mL) into H_2O_2 (20 mM) solutions. After designated times, the mixtures were centrifuged and the UV-Vis spectra of remaining H_2O_2 was recorded. The concentration of H_2O_2 was evaluated against a calibration curve, which was established by recording the UV-Vis spectra and the absorbance of various known concentrations of H_2O_2 (0-30 mM) at 240 nm.

Singlet oxygen generation by Au@Rh-ICG-CM nanocomposite

DPBF was used as a probe to detect the generation of reactive oxygen species (ROS) by Au@Rh-ICG-CM nanocomposites in the presence or absence of hydrogen peroxide upon 808-nm laser irradiation. DPBF can be easily oxidized by reactive oxygen species to change its structure, resulting in the decrease of its absorption at 410 nm. Typically, 50 μL of DPBF (1 mg/mL, dissolved in acetonitrile) was added to a dispersion of Au@Rh-ICG-CM. The absorbance of DPBF at 410 nm was measured and compared in the presence or absence of H_2O_2 (1×10^{-4} M) under an 808-nm laser irradiation (0.3 W/cm^2).

Furthermore, the intracellular singlet oxygen level was also determined using SOSG. In the presence of singlet oxygen, SOSG could generate an endoperoxide product, which emitted bright green fluorescence to indicate the intracellular singlet oxygen levels. To test the generation of singlet oxygen in a normoxic environment, MDA-MB-231 cells were incubated with either free ICG or Au@Rh-ICG-CM solutions (100 μg/mL) at 37 °C, 5% CO_2 under air condition for 6 h. To test the generation of singlet oxygen in a hypoxic environment, the cells were treated with either Au@Rh-CM or Au@Rh-ICG-CM under N_2 condition for 6 h. After washing the cells with PBS, SOSG (10 μM) mixed with or without H_2O_2 (1 mL, 1×10^{-4} M, a pathophysiological concentration identified in the native tumor) was added into the culture and incubated for 30 min in the air or N_2 environment. Then, the cells were washed twice with PBS

to remove excess SOSG. Finally, the cells were irradiated with the 808-nm (0.3 W/cm^2) laser for 3 min and fluorescence images of the cells were obtained with an epi-fluorescence microscope at an excitation wavelength of 480 ± 15 nm and emission wavelength of 535 ± 20 nm.

Cellular uptake of Au@Rh-ICG-CM nanocomposite

MDA-MB-231 cells were trypsinized to obtain cell suspensions and then replanted into 6-well plates with 10^6 cells/well. After culture for 24 h, the medium was replaced with Au@Rh-ICG-CM solutions or free ICG solution with the same content as Au@Rh-ICG-CM. After 6 h, the cells were washed with PBS for three times to remove excess nanoparticles or ICG and then fixed with 10% formalin prior to 4′,6-diamidino-2-phenylindole (DAPI) staining. The stained cells were observed with an epifluorescence microscope at an excitation wavelength of 560 ± 20 nm and an emission wavelength of 630 ± 30 nm for ICG and at an excitation wavelength of 360 ± 20 nm and an emission wavelength of 460 ± 25 nm for DAPI.

To further determine the intracellular destination of Au@Rh-ICG-CM nanocomposites in the tumor cells, MDA-MB-231 cells (1×10^6 cells per well) were seeded into 6-well plates and incubated with Au@Rh-ICG-CM nanocomposite (100 μg/mL) for 6 h. Then, the cells were washed three times with PBS, trypsinized and centrifuged to obtain the cell pellets. The pellets were fixed with the glutaraldehyde formaldehyde for 24 h and post fixed with osmium tetroxide for 1 h after PBS washing. After further rinsing with distilled water, the pellets were dehydrated in a series of graded ethanol solutions and embedded in epoxy for 24 h. Thin sections (60 nm) of the embedded pellets were cut and then observed under the TEM.

To evaluate the homologous targeting effect of Au@Rh-ICG-CM**,** GFP-labeled human umbilical vein endothelial cells (HUVECs) and non-labelled MDA-MB-231

cells (1×10^6 cells in total per well) were co-cultured into 6-well plates and incubated with Au@Rh-ICG-CM or free ICG (100 μg/mL). Then, the cells were washed with PBS for three times to remove excess nanoparticles or ICG and then fixed with 10% formalin prior to 4′,6-diamidino-2-phenylindole (DAPI) staining. The stained cells were observed with an epi-fluorescence microscope at an excitation wavelength of 560 ± 20 nm and an emission wavelength of 630 ± 30 nm for ICG, an excitation wavelength of 360 ± 20 nm and an emission wavelength of 460 ± 25 nm for DAPI, and an excitation wavelength of 480 ± 15 nm and an emission wavelength of 535 ± 20 nm for GFP. To further quantitatively confirm the homologous targeting effect, co-cultured HUVECs (GFP-labeled) and MDA-MB-231 (non-fluorescently labeled) upon various treatments (PBS, free ICG and Au@Rh-ICG-CM) were analyzed with an Attune® acoustic focusing flow cytometer (Thermo Fisher).

O_2 generation of Au@Rh-ICG-CM

The intracellular production of O_2 was investigated using an oxygen indicator, RDPP. As the degree of hypoxia increases, the intensity of red fluorescence of RDPP also proportionally increases. Briefly, MDA-MB-231 cells were incubated with Au@Rh-ICG-CM (100 μg/mL) for 6 h in the N_2 atmosphere. Upon discarding the medium, cells were rinsed carefully with PBS and incubated with RDPP probe for 30 min. The cells were then examined using an epi-fluorescence microscope at an excitation wavelength of 560 ± 20 nm and an emission wavelength of 630 ± 30 nm.

***In vitro* antitumor performance**

The cell-killing effect of Au@Rh-ICG-CM was measured by MTT assay. Briefly, MDA-MB-231 cells seeded and cultured in 96-well plates for 24 h at 37 °C were respectively treated with Au@Rh-CM and Au@Rh-ICG-CM at gradient concentrations. After incubation for another 18 h, the cells were irradiated with an 808 nm laser (0.3

W/m^2) for 3 min under normoxia. The cytotoxicity assay under hypoxia was the same as that for normoxia except that the cells were cultured in the N_2 atmosphere. The cells were cultured for another 6 h and then 20 μL of MTT (5 mg/mL in PBS) was added to each well and then incubated for another 4 h. Upon removal of the media, 150 μL of DMSO was added to extract the formazan under gently shaking for 5 minutes, and the optical density (OD) at 590 nm was recorded by a microplate reader.

Live and dead staining (*i.e.*, calcein-AM/PI) was also performed to study the *in vitro* anti-tumor activity of Au@Rh-ICG-CM under the N_2 atmosphere. The MDA-MB-231 cells seeded into 6-well plates were treated with Au@Rh-CM or Au@Rh-ICG-CM with or without H_2O_2 (1×10^{-4} M, the pathophysiological concentration of native tumors) in the absence or presence of 808-nm laser irradiation (0.3 W/cm^2, 3 min). The resulting cells were stained with calcein-AM/PI and examined under an epi-fluorescence microscope.

Establishment of tumor xenograft model

Female Balb/c nude mice (6-8 weeks old, ~20 g) were purchased from the Department of Experimental Animals, Xiamen University and maintained under standard housing conditions. Subcutaneous MDA-MB-231 tumors were generated by subcutaneous injection of MDA-MB-231 cells (2×10^6) suspended in 100 μL of PBS on the back of each female Balb/c mice. When the tumor volume reached ~80 mm^3, the mice were used for *in vivo* experiments. All animal experiments were carried out in accordance with the guidelines evaluated and approved by the ethics committee of Xiamen University.

***In vivo* fluorescence and photoacoustic imaging**

For *in vivo* fluorescence imaging, Au@Rh-ICG-CM (100 μL, 1 mg/mL) was intravenously (*i.v.*) injected into the tail vein of MDA-MB-231 tumor-bearing Balb/c

nude mice. Fluorescence images at 0, 2, 4, 8, 12, and 24 h were acquired using an *in vivo* imaging system (IVIS Lumina II, PerkinElmer). After 24 h *in vivo* imaging, all mice were euthanized. Tumors and major organs including heart, liver, spleen, lung and kidneys were collected and subjected to *ex vivo* imaging.

For photoacoustic (PA) imaging, Au@Rh-ICG-CM at a concentration of 1 mg/mL was *i.v.* injected into the MDA-MB-231 tumor-bearing mice. The tumor region was imaged at different time points *via* a visual sonic system (VisualSonics Vevo 2100 LAZER systems) with an excitation wavelength at 808 nm.

***In vivo* therapeutic effect of Au@Rh-ICG-CM**

In order to investigate the *in vivo* therapeutic effect of Au@Rh-ICG-CM, MDA-MB-231 tumor-bearing mice were stochastically divided into five groups (n = 5): (1) PBS, (2) laser only, (2) Au@Rh-ICG-CM (1 mg/mL, 100 μL), (4) Au@Rh-CM (1 mg/mL, 100 μL) + laser, and (5) Au@Rh-ICG-CM (1 mg/mL, 100 μL) + laser. 12 h after tail intravenous injection of nanostructures, the tumor areas of the mice were exposed to an 808-nm laser irradiation (0.3 W/cm^2) for 5 min. The mice with *i.v.* injected PBS and Au@Rh-ICG-CM were used for infrared thermal imaging. During therapeutic treatment, the mice received various treatments *via i.v.* injection every 2 days. At 12 h post-injection, the mice were irradiated with 808-nm laser (0.3 W/cm^2) for 5 min. In addition, the tumor volume and body weight of the mice were also recorded every 2 days up to 16 days. The tumor volume was calculated according to the following formula: tumor volume = length × width^2/2. By the time of sacrificing, the tumors and all major organs were collected and processed for histologic analysis after H&E staining.

Immunofluorescence staining

Immunofluorescence staining was performed on thin frozen sections of tissues for

hypoxia inducible factor alpha (HIF-1α) and microvessels using anti mouse-HIF-1α and anti-mouse CD31 monoclonal antibody, respectively, according to the protocol provided by the manufacturer. Upon incubation with primary antibody for 1 h, the sections were then incubated with a secondary antibody (Alexa Fluor 488-conjugated goat anti-mouse IgG antibodies, dilution 1:200, Jackson Inc.). The stained sections were examined with an epifluorescence microscope and representative images were captured. Images were then analyzed using the NIH ImageJ software (1.46r). The fluorescence positive area (%) was evaluated for HIF-α or CD31 over the area of tumor tissue. The production of ROS and $^1O_2$ in tumor tissues was also detected by fluorescence staining the tissue cross-sections with dihydroethidium (DHE) (20 mM, Invitrogen) and SOSG (100 μM, Fisher Scientific), respectively, and then examining with an epi-fluorescence microscope.

For the pimonidazole staining, the tumor-bearing mice were intraperitoneally injected with pimonidazole hydrochloride (60 mg kg^{-1}). After 1 h, the mice were sacrificed and tumors were harvested. Upon being snap-frozen, the tumor specimens were cut into thin sections (10 μm thick), post-fixed with cold acetone for 20 min, washed with ice-cold PBS and then blocked with 10% BSA overnight. The sections were incubated with FITC-conjugated mouse monoclonal antibody against pimonidazole (FITC-Mab1, dilution 1:200, Hypoxyprobe-1 Plus Kit, Hypoxyprobe Inc., Burlington) for 1 h at room temperature and then stained with DAPI. The stained sections were examined under an epi-fluorescence microscope and fluorescence images were captured.

Statistical analysis

All quantitative results were obtained from at least three samples. Data were presented as the mean ± SD. Each experiment was repeated at least three times (except

where noted). Data were analyzed by using GraphPad Prism statistical software (version 7.00). Comparisons of two groups were made with an unpaired Student's t-test. Statistical significance was set at *$p < 0.05$, **$p < 0.01$.

References

[1] B. Jiang, C. Li, O. Dag, H. Abe, T. Takei, T. Imai, M. S. A. Hossain, M. T. Islam, K. Wood, J. Henzie1, Y. Yamauchi, *Nature Commun.* **2017**, *8*, 15581.

[2] B. F. Roberts, *J. Colloid Interf. Sci.* **1967**, *23*, 266.

[3] L. Goth, *Clin. Chim. Acta* **1991**, *196*, 143-151.

[4] L. Feng, Z. Dong, C. Liang, M. Chen, D. Tao, L. Cheng, K. Yang, Z. Liu, *Biomaterials* **2018**, *181*, 81-91.

[5] J. Liu, Y. Liu, W. Bu, J. Bu, Y. Sun, J. Du, J. Shi, *J. Am. Chem. Soc.* **2014**, *136*, 9701.

Supporting Figures

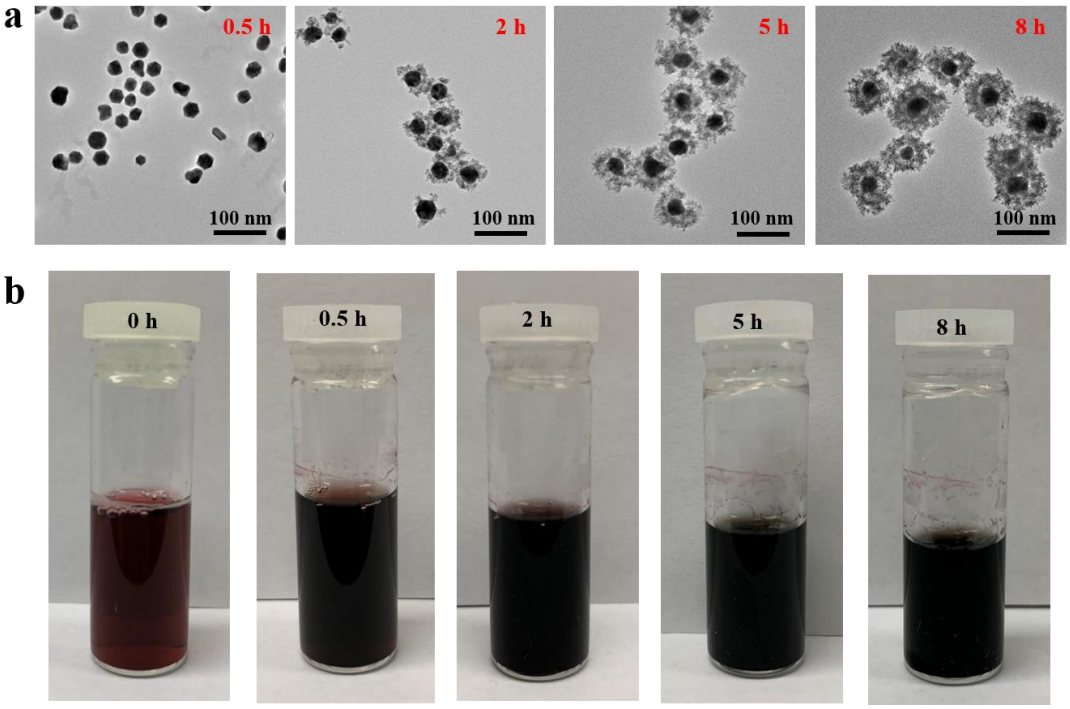

Figure S1. (a) TEM micrographs of Au@Rh nanostructures sampled from different reaction periods (0.5 h, 2 h, 5 h, and 8 h, respectively). (b) Photographs of the colloidal suspensions of reaction solutions at different reaction times. The reaction was carried out at 60 ^{o}C.

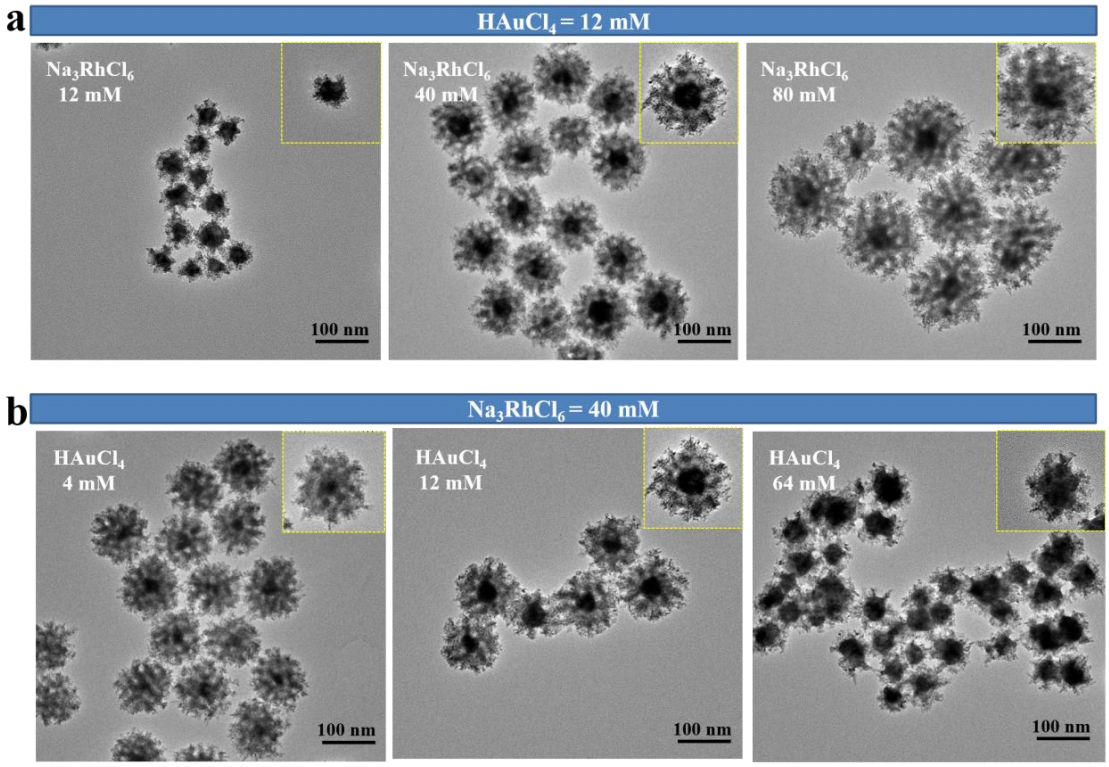

c

Amounts		Core size (nm)	Shell thickness (nm)	Mean particle size (nm)
$HAuCl_4$	Na_3RhCl_6			
	12 mM	33.5 ± 4.6	6.3 ± 1.2	40.5 ± 2.1
12 mM	40 mM	32.6 ± 3.9	30 .8 ± 2.5	95.6 ± 3.6
	80 mM	31.4 ± 5.3	43.7 ± 3.9	142.8 ± 3.2
4 mM		15.6 ± 2.1	36.3 ± 3.8	90.6 ± 2.5
12 mM	40 mM	32.6 ± 3.9	30 .8 ± 2.5	95.6 ± 3.6
64 mM		50.6 ± 6.6	15.5 ± 3.4	70.2 ± 1.9

Figure S2. TEM micrographs of the Au@Rh core-shell nanostructures prepared from Au and Rh precursors at different ratios. (a) With the concentration of $HAuCl_4$ fixed at 12 mM, the Na_3RhCl_6 amount was varied (12 mM, 40 mM, and 80 mM). (b) With the concentration of Na_3RhCl_6 fixed at 40 mM, the $HAuCl_4$ amount was varied (4 mM, 12 mM, and 64 mM). The experiments were performed for three times, and representative images are presented in (a) and (b). (c) Summary of the core size, shell thickness, and mean diameters of the nanostructures obtained from different conditions. The molar

concentration of $HAuCl_4$ and Na_3RhCl_6 refers to that in 2 mL of mixed solution. The Data presented (mean ± SD) were measured from TEM images by Image J (n > 50 particles).

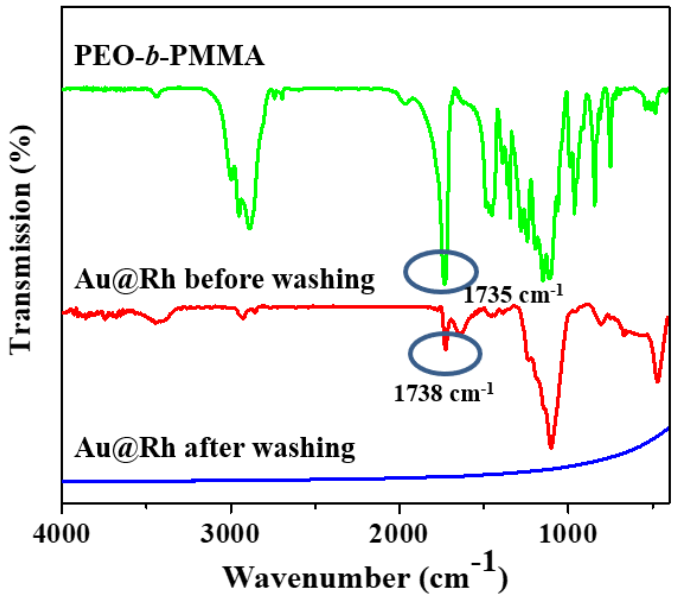

Figure S3. FTIR spectra of the porous Au@Rh core-shell nanostructures before and after the washing step.

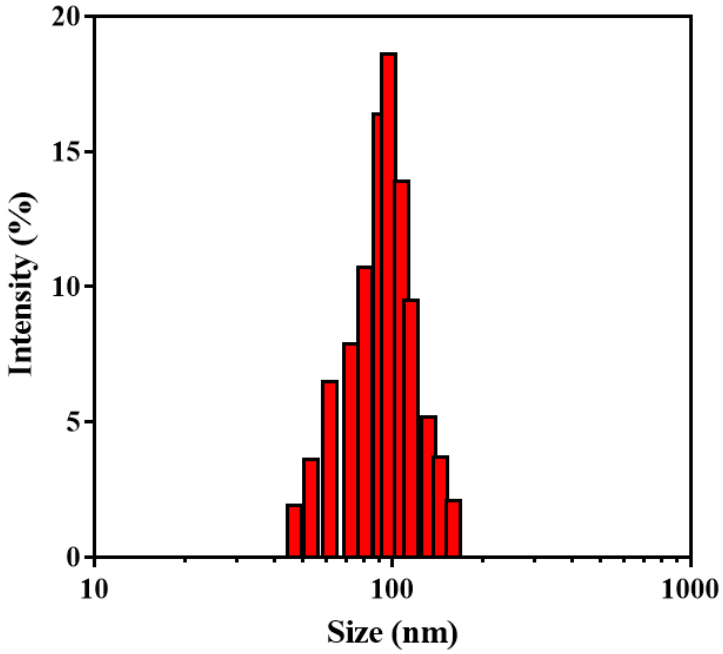

Figure S4. Size distribution of porous Au@Rh core-shell nanostructures.

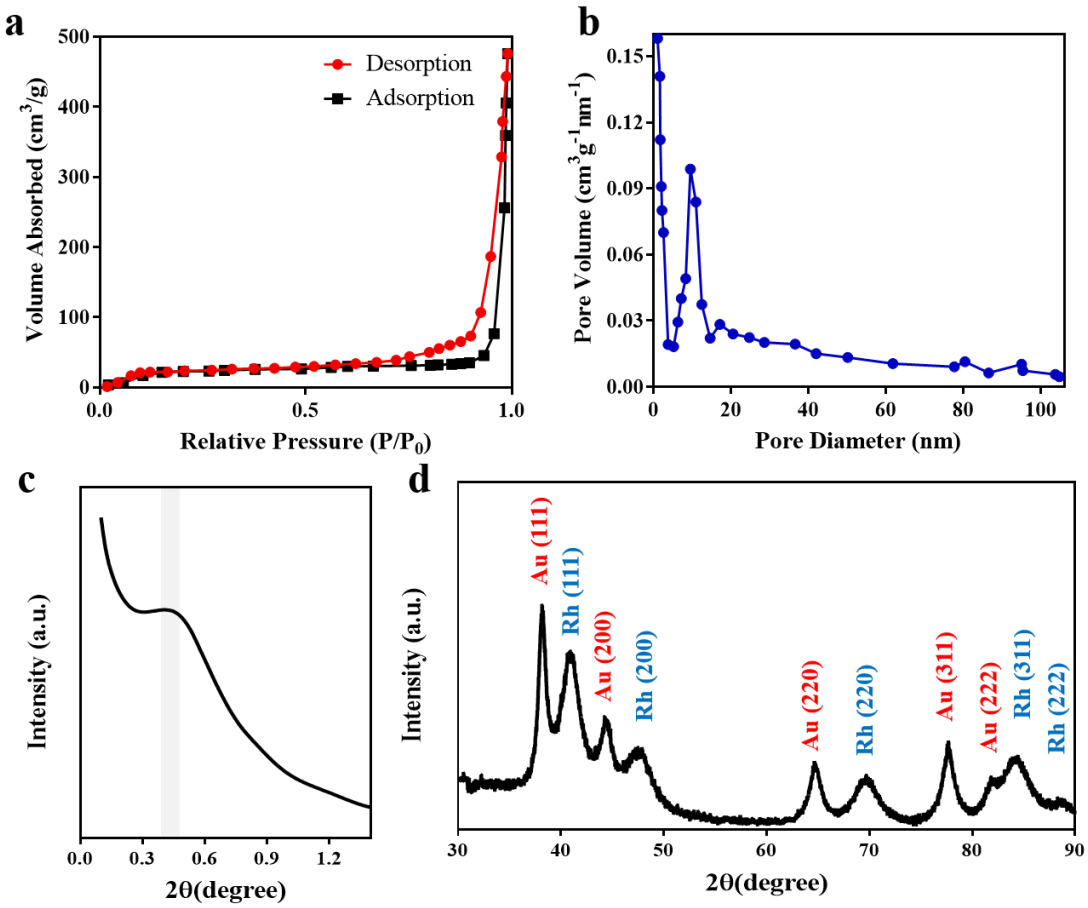

Figure S5. N_2 adsorption/desorption isotherm (a) and the corresponding pore-size distribution curves (b) of porous Au@Rh core-shell nanostructures. (c) Low-angle and (d) wide-angle XRD patterns of the mesoporous biphasic and bimetallic Au@Rh nanostructures.

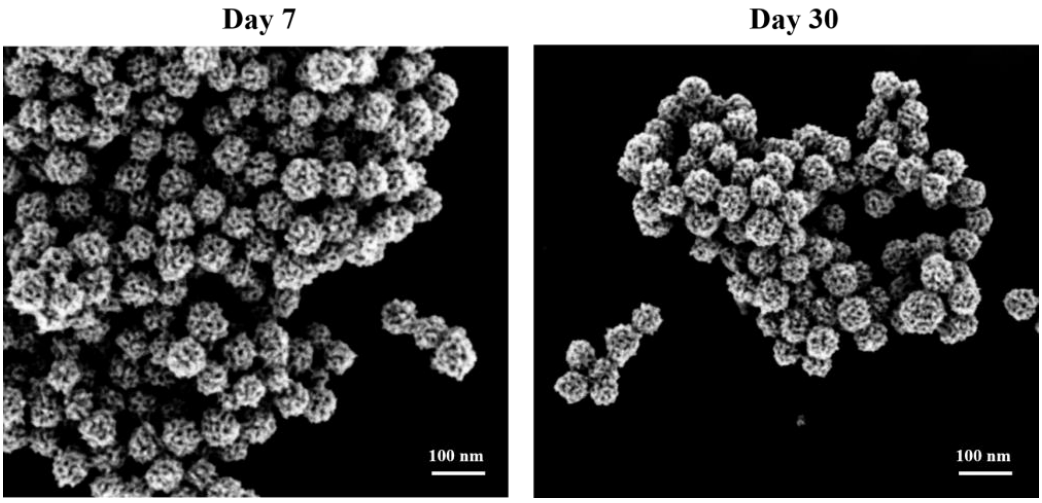

Figure S6. SEM micrographs of the mesoporous Au@Rh nanoparticles after storage at room temperature for 7 and 30 days, respectively.

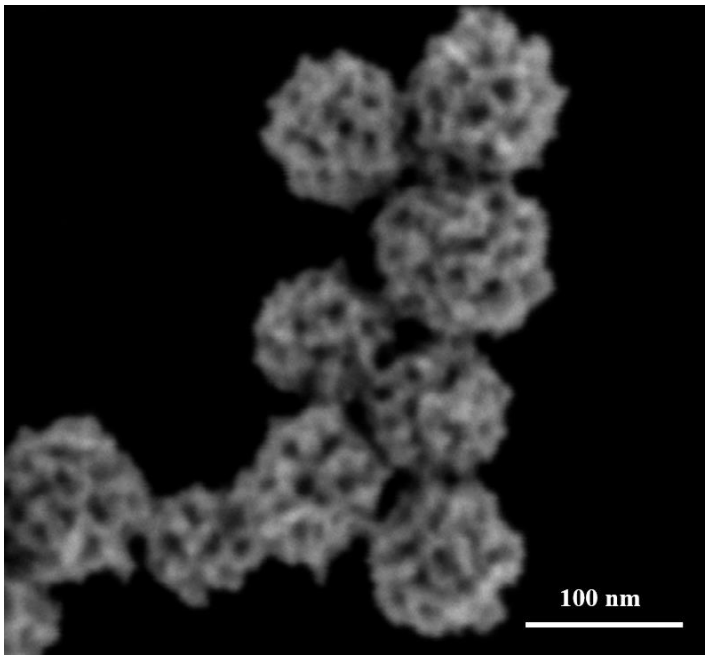

Figure S7. SEM micrograph of the mesoporous Au@Rh nanostructures at a high magnification.

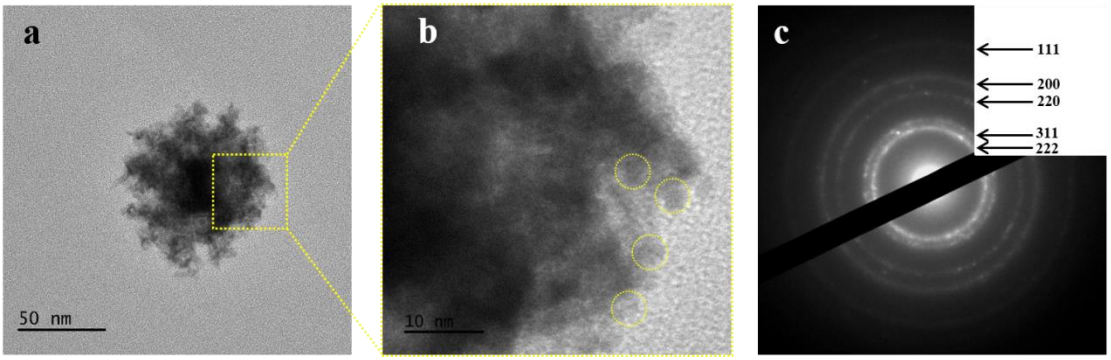

Figure S8. (a) TEM micrograph of a single mesoporous Au@Rh nanostructure. (b) HRTEM micrograph of the mesoporous Au@Rh nanostructure. (c) SAED pattern obtained from the single Au@Rh nanostructure in (a).

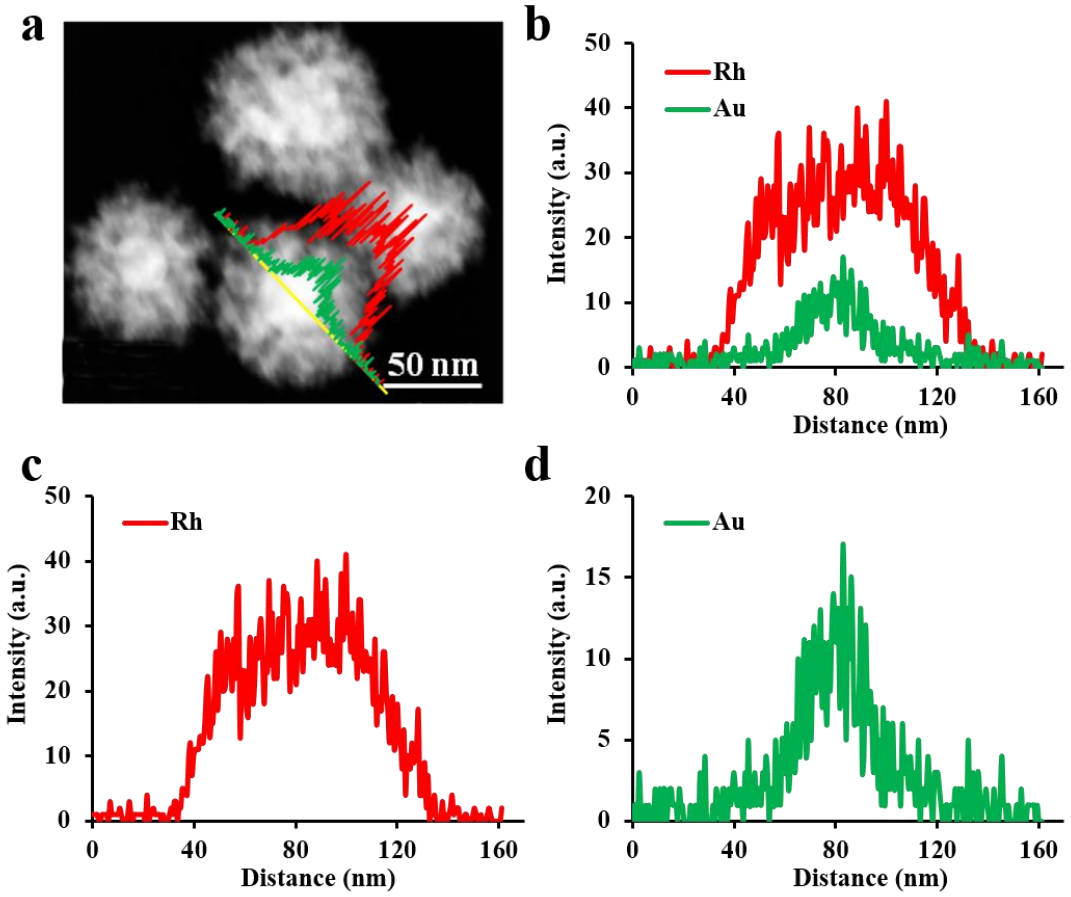

Figure S9. TEM micrographs (a) and the corresponding EDS line scans (b) with individual Rh (c) and Au (d) signal of the core-shell Au@Rh nanostructures.

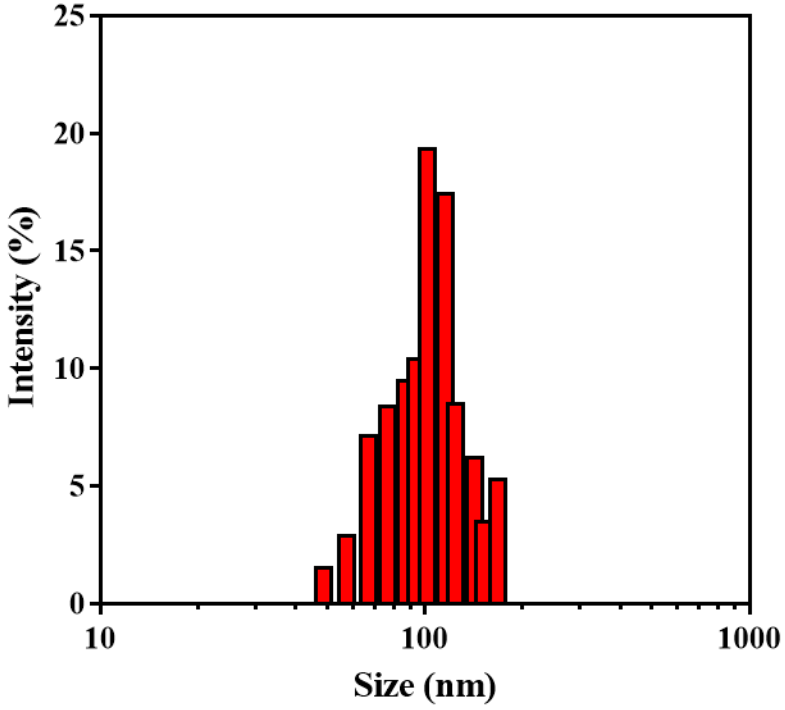

Figure S10. Size distribution of Au@Rh-CM nanoparticles.

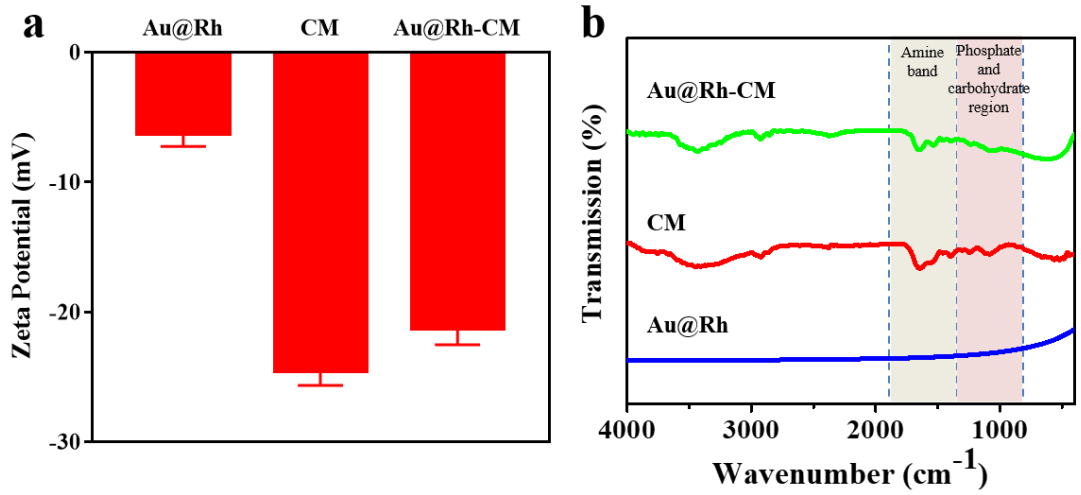

Figure S11. (a) Zeta potentials and (b) FTIR spectra of Au@Rh, CM and Au@Rh-CM.

Data in (a) are shown as mean ± SD (n = 3).

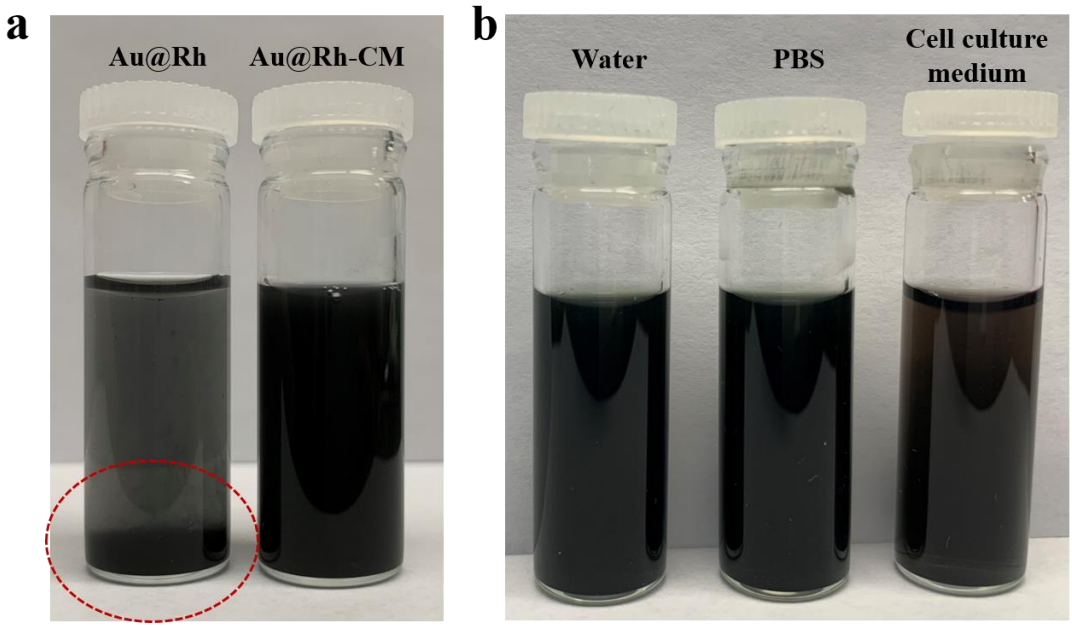

Figure S12. (a) Photos of Au@Rh and Au@Rh-CM nanostructures in D.I. water after 30 days. Red circle indicates the precipitate. (b) Photos of Au@Rh-ICG-CM nanostructures in D.I. water, PBS, and cell culture medium after 30 days.

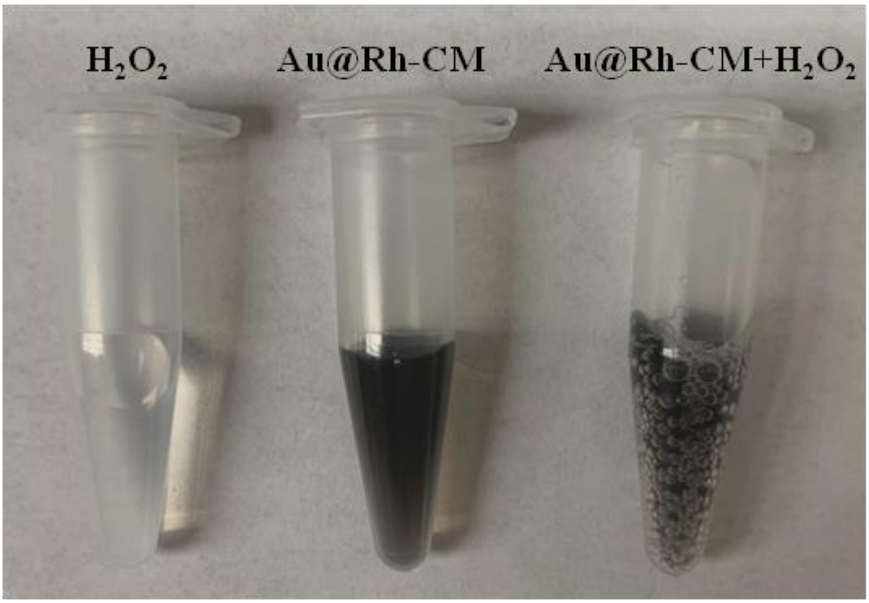

Figure S13. Photos of the tubes containing H_2O_2, Au@Rh-CM, and Au@Rh-CM + H_2O_2. Oxygen bubbles were seen in the tube with Au@Rh-CM + H_2O_2.

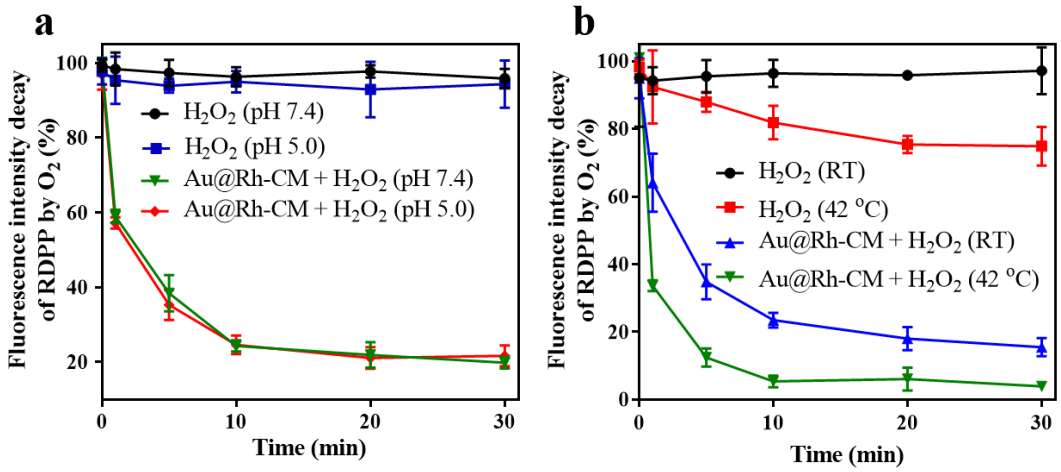

Figure S14. (a) Oxygen generation in relation to the pH change in different systems [H_2O_2 (pH 7.4), H_2O_2 (pH 5.0), Au@Rh-ICG-CM + H_2O_2 (pH 7.4) and Au@Rh-ICG-CM + H_2O_2 (pH 5.0)]. Data are shown as mean ± SD (n = 3). (b) Oxygen generation in relation to the temperature change in different systems [H_2O_2 (RT), H_2O_2 (42 °C), Au@Rh-ICG-CM + H_2O_2 (RT) and Au@Rh-ICG-CM + H_2O_2 (42 °C)]. Data are shown as mean ± SD (n = 3).

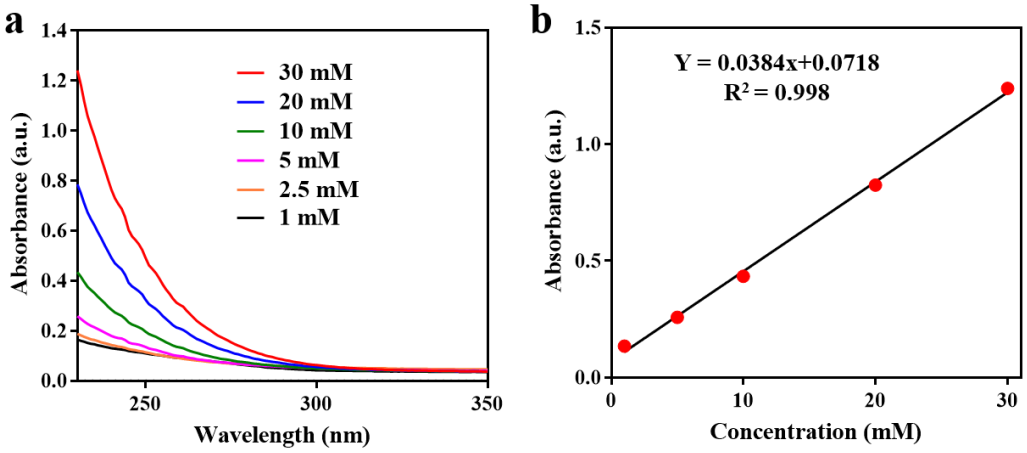

Figure S15. (a) The UV-Vis spectra of H_2O_2 (1, 2.5, 5, 10, 20, 30 mM). b) The calibration curve of absorbance at 240 nm as a function of the concentration of H_2O_2. Experiments were repeated three times independently.

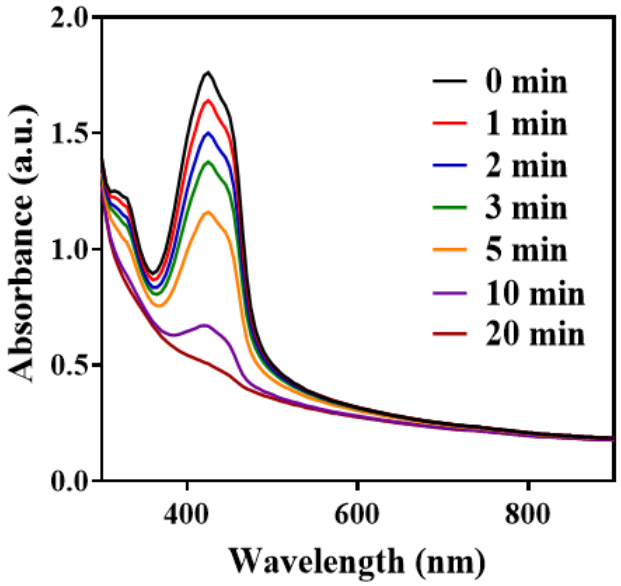

Figure S16. Time-dependent UV-vis-NIR spectra of the mixture of Au@Rh-ICG-CM and DPBF under 808-nm laser irradiation (0.3 W/cm^2).

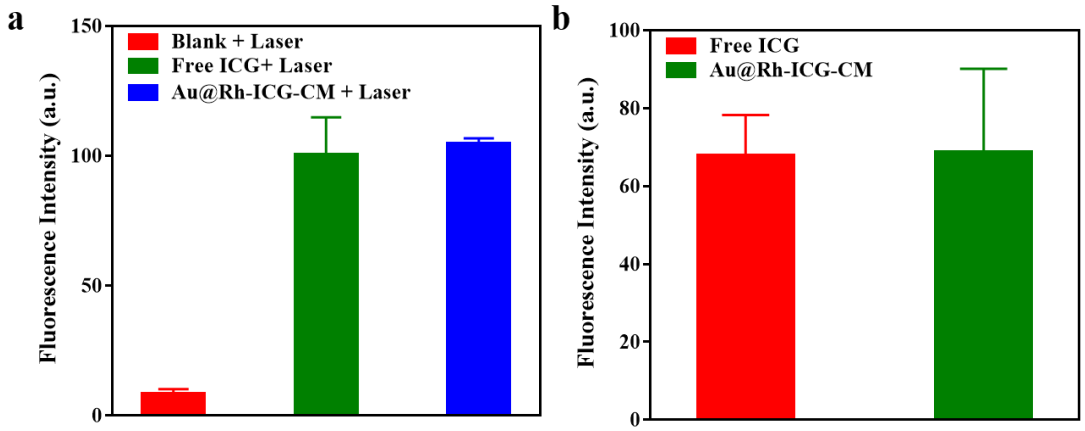

Figure S17. (a) Semi-quantification of SOSG fluorescence intensity in MDA-MB-231 cells treated with free ICG or Au@Rh-ICG-CM nanocomposites under laser irradiation (808 nm, 0.3 W/cm^2, 3 min). Fluorescence images of cells stained with SOSG for singlet oxygen as recorded from more than five images for each group were analyzed using Image J (NIH). Data are shown as mean ± SD. (b) Semi-quantification of ICG fluorescence intensity in MDA-MB-231 cells incubated for 6 h with free ICG or Au@Rh-ICG-CM. Fluorescence images of cells as recorded from more than five images for each group were analyzed using Image J (NIH). Data are shown as mean ± SD.

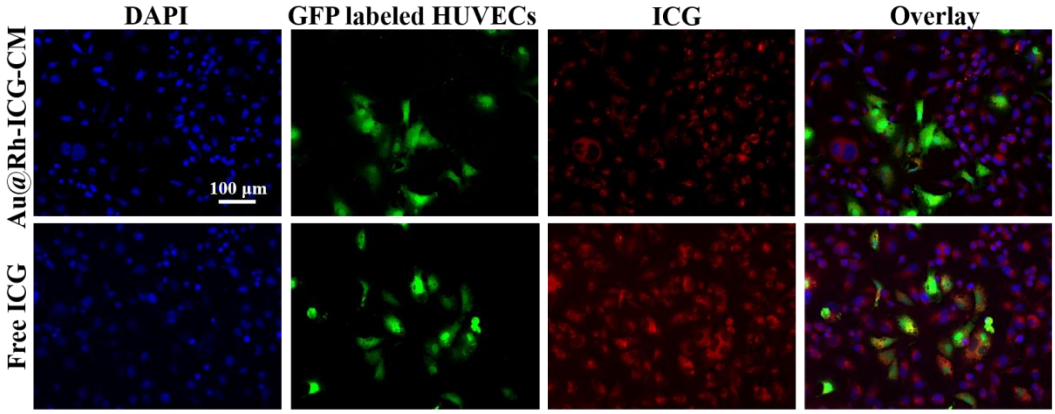

Figure S18. Fluorescence images of co-cultured MDA-MB-231 cells and GFP-labeled HUVECs after respective incubation with Au@Rh-ICG-CM and free ICG. The experiment was performed three times for each group, and representative images are presented.

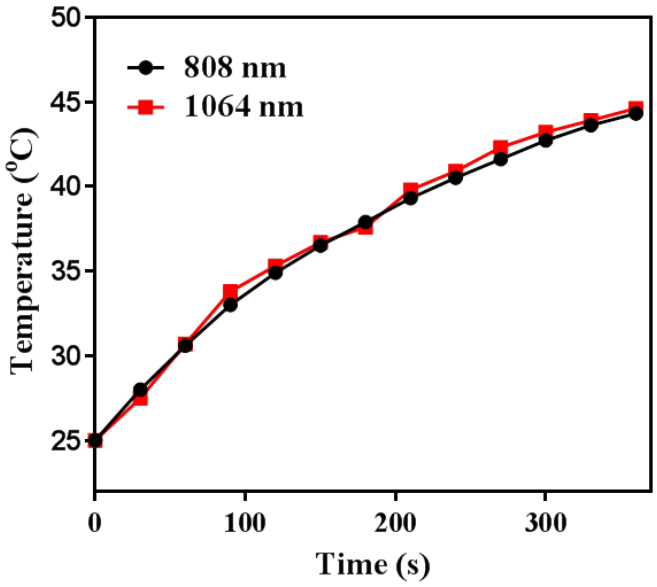

Figure S19. Heating curves of Au@Rh-ICG-CM under 808-nm or 1064-nm laser irradiation.

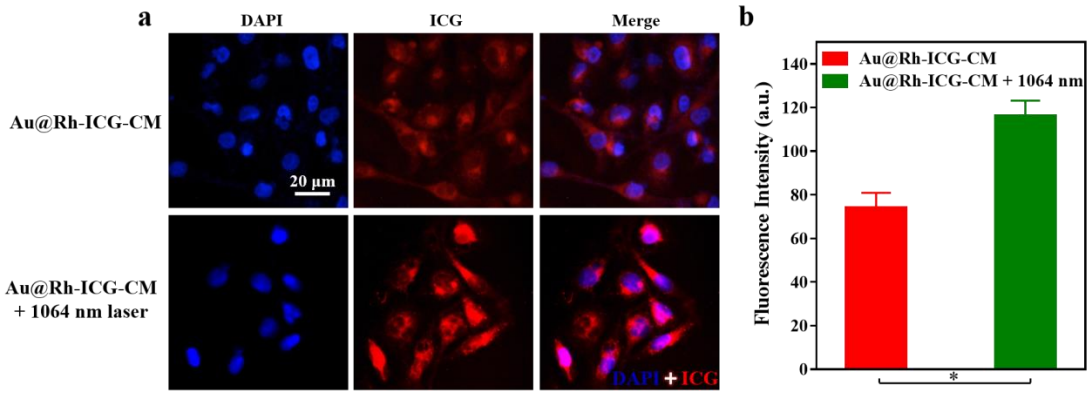

Figure S20. (a) Fluorescence images of MDA-MB-231 cells after incubation with Au@Rh-ICG-CM and 3 min of laser irradiation (1064 nm, 0.6 W/cm^2). The experiment was performed three times for each group, and representative images are presented. (b) Semi-quantification of ICG fluorescence intensity in MDA-MB-231 cells after incubation with Au@Rh-ICG-CM and laser irradiation (1064 nm, 0.6 W/cm^2, 3 min). Fluorescence images of cells as recorded from more than five images for each group were analyzed using ImageJ (NIH). Data are shown as mean ± SD. Statistical significance was assessed by unpaired Student's t-test. *$P < 0.05$.

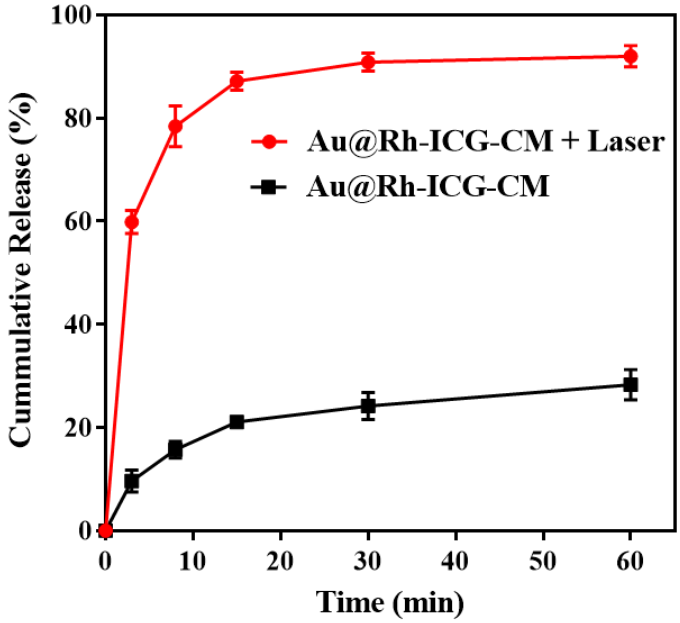

Figure S21. ICG release from the Au@Rh-ICG-CM with or without 1064-nm laser irradiation (0.6 W/cm^2) for 0, 3, 8, 15, 30 min. Data are shown as mean ± SD (n = 3).

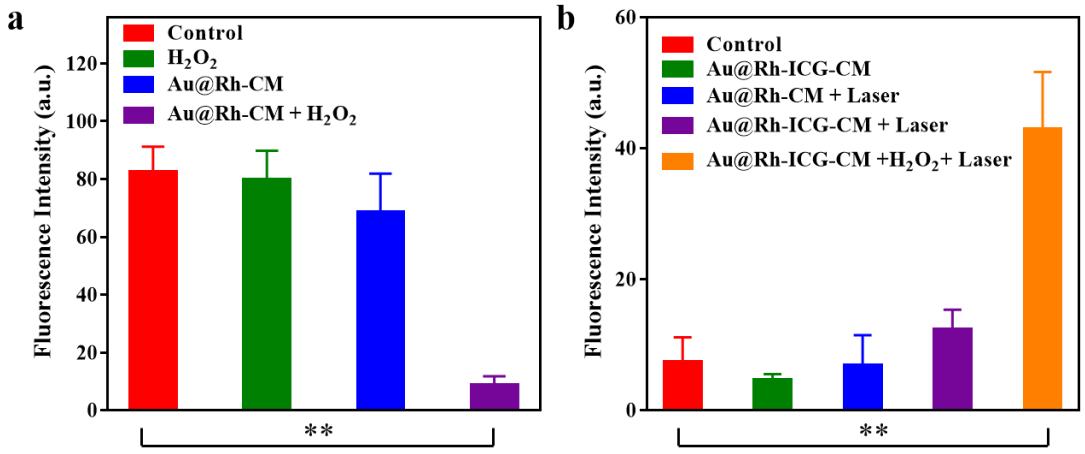

Figure S22. (a) Semi-quantification of the RDPP fluorescence intensity in MDA-MB-231 cells in a hypoxic setting (*i.e.*, N_2 atmosphere) after various treatments (non-treated control, H_2O_2, Au@Rh-CM, or Au@Rh-CM + H_2O_2). Fluorescence images of cells ($n \geq 5$ for each group) were analyzed by ImageJ (NIH). Data are shown as mean ± SD. Statistical significance was assessed by unpaired Student's t-test. *$p < 0.05$, **$p < 0.01$. (b) Semi-quantification of the SOSG fluorescence intensity in MDA-MB-231 cells in N_2 atmosphere after various treatments (non-treated control, Au@Rh-ICG-CM in dark, Au@Rh-CM with 808-nm laser irradiation, Au@Rh-ICG-CM with 808-nm laser irradiation, or Au@Rh-ICG-CM + H_2O_2 with 808-nm laser irradiation). Irradiation time was 3 min. Fluorescence images of cells ($n \geq 5$ for each group) were analyzed by ImageJ (NIH). Data are shown as mean ± SD. Statistical significance was assessed by unpaired Student's t-test. *$p < 0.05$, **$p < 0.01$.

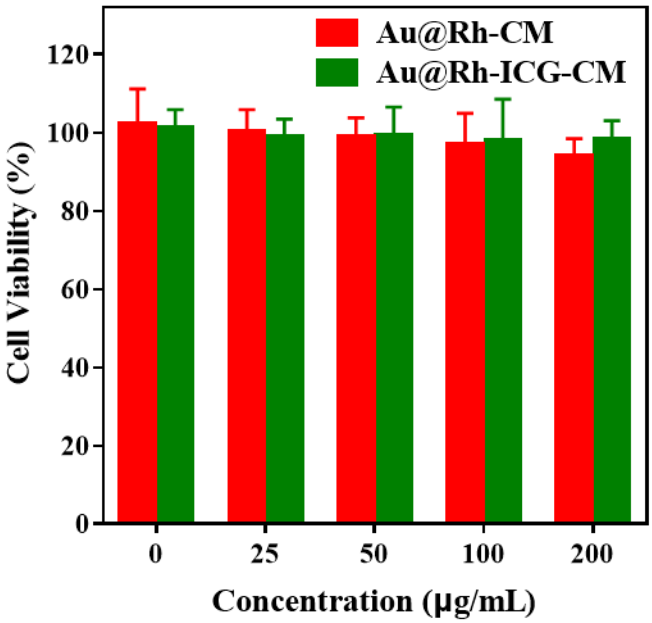

Figure S23. *In vitro* cytocompatibility of Au@Rh-CM or Au@Rh-ICG-CM with MDA-MB-231 cells under normoxia (air atmosphere). Data are shown as mean ± SD (n = 6).

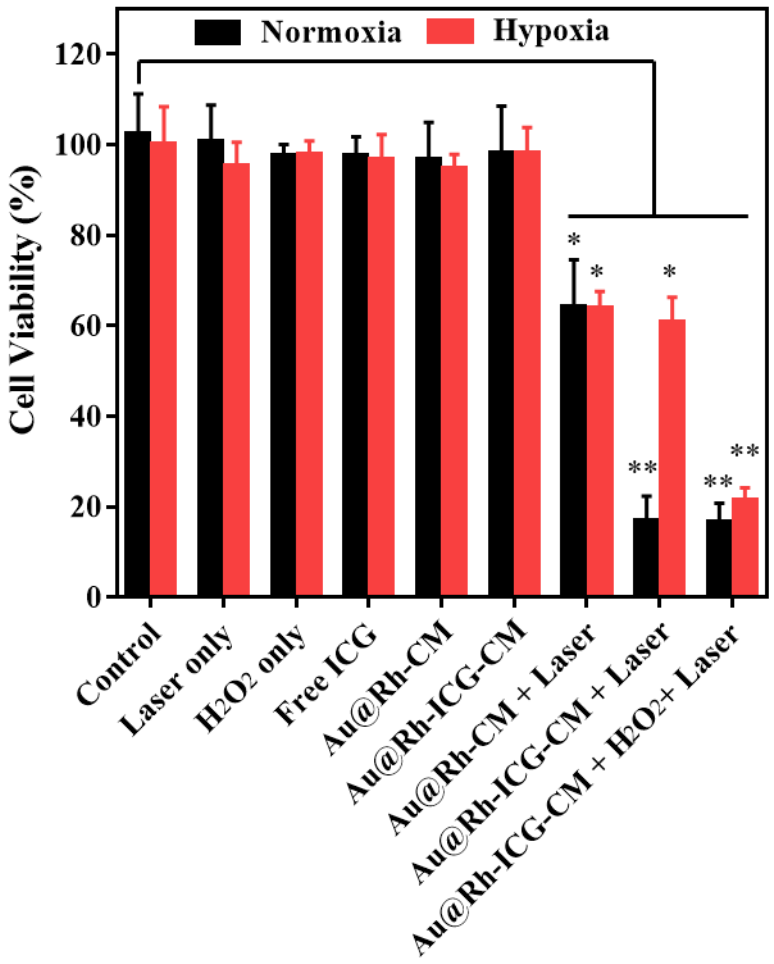

Figure S24. Cell killing efficacy of different treatments to MDA-MB-231 cells without or with 808-nm laser irradiation (0.3 W/cm^2, 3 min) under normoxia or hypoxia. Data are shown as mean ± SD (n = 6). Statistical significance was assessed by unpaired Student's t-test. *$p < 0.05$, **$p < 0.01$.

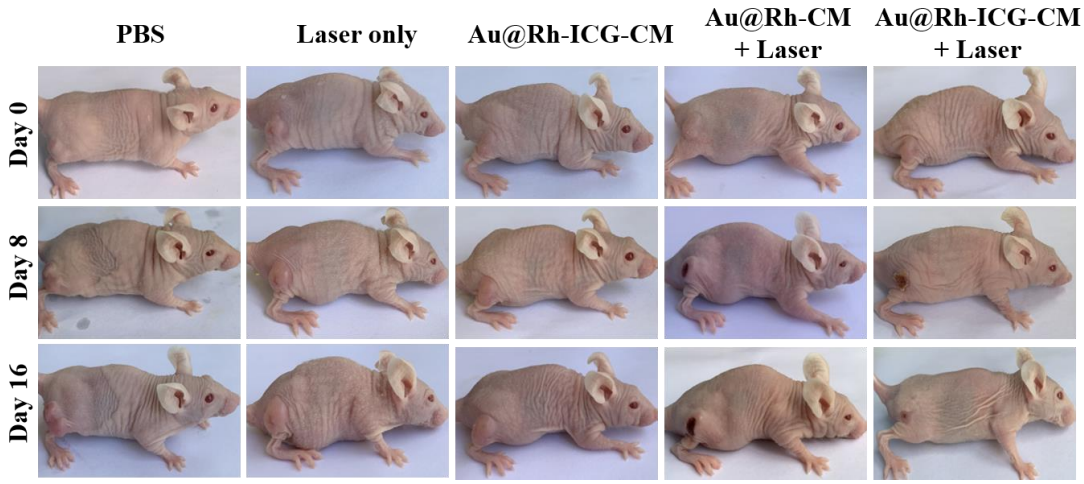

Figure S25. Photos of tumors from different treatment groups (PBS, laser only, Au@Rh-ICG-CM, Au@Rh-CM plus 808-nm laser and Au@Rh-ICG-CM plus 808-nm laser) at different time points (day 0, 8 and 16). Each observation was performed on five parallel samples collected from different mice after treatment, and representative photos are presented.

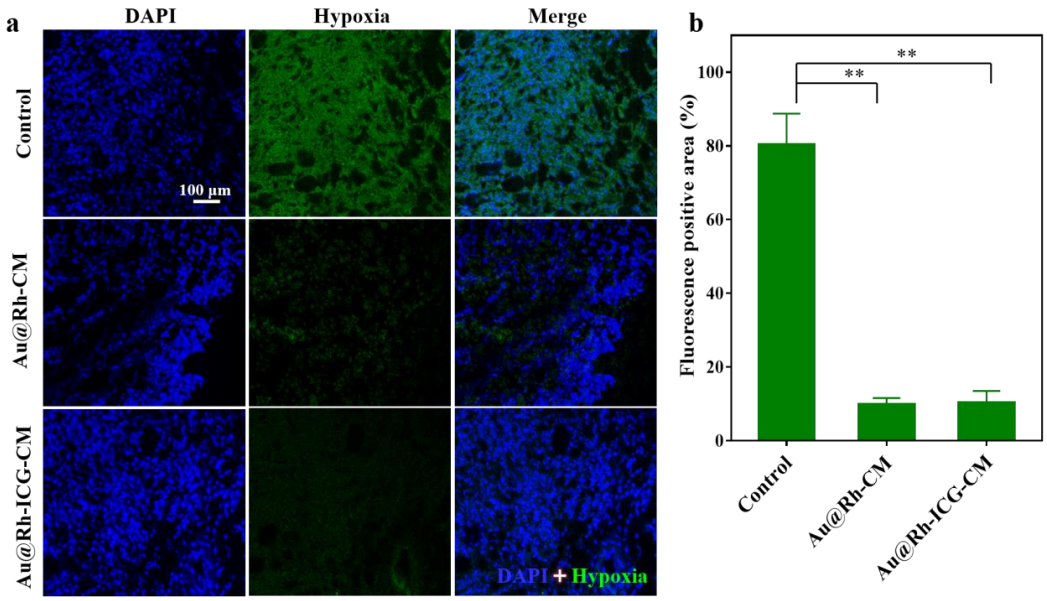

Figure S26. (a) Representative immunofluorescence images of tumor sections stained with the hypoxia-probe. The nuclei and hypoxic areas were stained with DAPI (blue), and anti-pimonidazole antibody (green), respectively. The experiment was performed three times for each group, and representative images are presented. (b) Semi-quantification of the hypoxic tumor area from different groups shown in (a). Fluorescence images ($n \geq 5$ for each group) were analyzed by ImageJ (NIH). Data are shown as mean ± SD. Statistical significance was assessed by unpaired Student's t-test. $^{**}p < 0.01$.

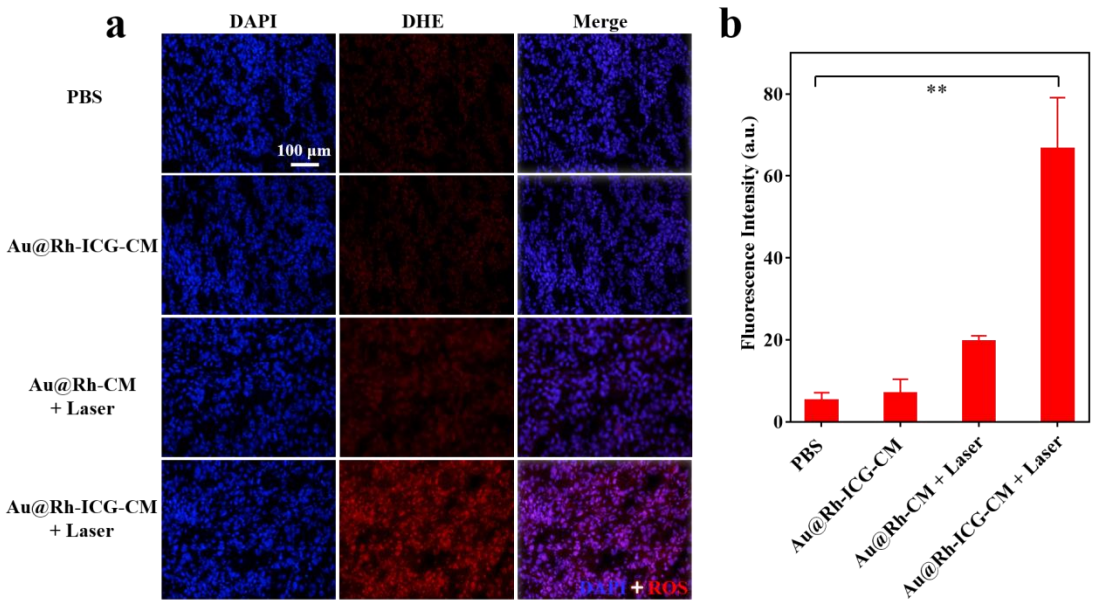

Figure S27. (a) Fluorescence images of different groups showing production of reactive oxygen species by DHE staining. The experiment was performed three times for each group, and representative images are presented. (b) Semi-quantification of the DHE fluorescence signal from different groups shown in (a). Fluorescence images ($n \geq 5$ for each group) were analyzed by ImageJ (NIH). Data are shown as mean ± SD. Statistical significance was assessed by unpaired Student's t-test. $^{**}p < 0.01$.

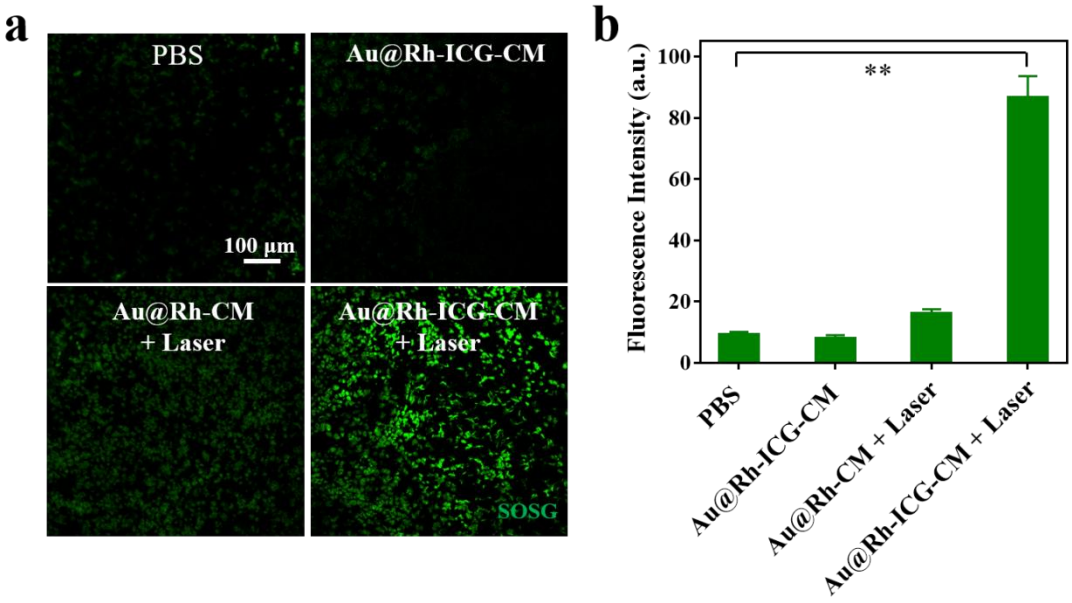

Figure S28. (a) Fluorescence images of singlet oxygen presented in tumor sections from different treatment groups upon SOSG staining. The experiment was performed three times for each group, and representative images are presented. (b) Semi-quantification of SOSG fluorescence signal from different groups shown in (a). Fluorescence images ($n \geq 5$ for each group) were analyzed by ImageJ (NIH). Data are shown as mean ± SD. Statistical significance was assessed by unpaired Student's t-test. $^{**}p < 0.01$.

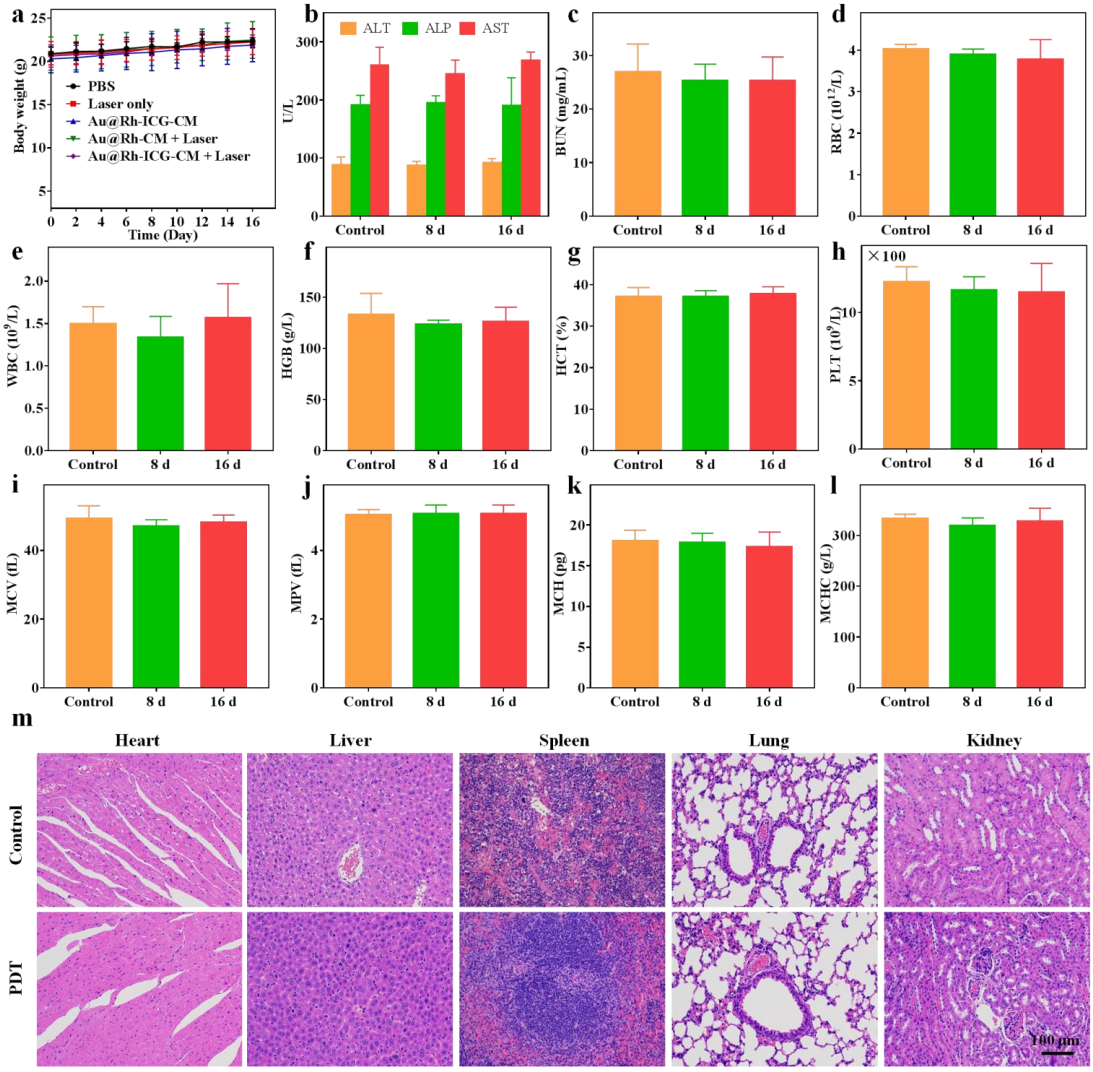

Figure S29. (a) Time-dependent changes in average body weight of MDA-MB-231 tumor-bearing mice within 16 days after different treatments. Data are expressed as mean ± SD (n = 5). (b) The levels of liver function markers (AST, ALP, and ALT) and of (c) kidney function marker (BUN) in mice before treatment (control) and after treatment with Au@Rh-ICG-CM at 7 and 15 days. Data in (b) and (c) are shown as mean ± SD (n = 3). (d-l) Routine blood data of mice before treatment (control) and after treatment with Au@Rh-ICG-CM at 7 and 15 days. Data are shown as mean ± SD (n = 3). (m) Histologic analysis of major organs including heart, liver, spleen, lung, and kidney from mice before treatment (control) and after treatment with Au@Rh-ICG-CM plus 808-nm laser irradiation. Cross-sections (7 μm) of tissues were stained with

hematoxylin and eosin (H&E). Each observation was performed on five parallel samples collected from different mice after treatment, and representative images are presented.

Supporting Table

Table S1

Characterization of Au@Rh-CM for the mean size and polydispersity index (PDI) after storage in various solutions (D. I. water, PBS and culture medium) at 4 ºC for 0, 7 and 30 days.

Samples		Size (nm)	PDI
In PBS	0 day	105.3 ± 1.4	0.121
	7 day	102.7 ± 3.1	0.201
	30 day	104.5 ± 2.9	0.103
In D.I. water	0 day	104.9 ± 2.8	0.152
	7 day	99.2 ± 1.9	0.183
	30 day	105.5 ± 2.4	0.119
In cell media	0 day	103.1 ± 2.3	0.129
	7 day	110.6 ± 3.9	0.156
	30 day	107.8 ± 4.2	0.204

Values are presented as the mean ± SD (n = 3).